De novo Design Protein Binders Targeting the Hydrophobic Surface of DENV4 and ZIKV NS1 Dimer

Qi Pan[1,2,6], Geshu Zhang[1,6], Jianhai Yu[3], Wanqin Zhang[1], Shiqi Zhuang[4,5], Jingchuan Xue[4], Wei Zhao[3], Hongli Hu[1,*], Haizhan Jiao[1,*].

[1]Department of Biomedical Sciences, Kobilka Institute of Innovative Drug Discovery, Division of Biomedical Health Sciences, School of Medicine, The Chinese University of Hong Kong, Shenzhen 518172, China

[2]Institute for Hepatology, National Clinical Research Center for Infectious Disease, Shenzhen Third People's Hospital, Department of Biochemistry，the Second Affiliated Hospital, School of Medicine, Southern University of Science and Technology, Shenzhen 518112, Guangdong Province, China.

[3]BSL-3 Laboratory (Guangdong), Guangdong Provincial Key Laboratory of Tropical Disease Research, School of Public Health, Southern Medical University, Guangzhou, Guangdong, 510515, China.

[4]Guangdong Basic Research Center of Excellence for Ecological Security and Green Development, Key Laboratory for City Cluster Environmental Safety and Green Development of the Ministry of Education, School of Ecology, Environment and Ocean, Guangdong University of Technology, Guangzhou, 510006, China

[5]Guangdong Provincial Key Laboratory of Water Quality Improvement and Ecological Restoration for Watersheds, Institute of Environmental and Ecological Engineering, Guangdong University of Technology, Guangzhou, 510006, China

[6]These authors contributed equally: Qi Pan, Geshu Zhang

[*]Correspondence e-mail: honglihu@cuhk.edu.cn, jiaohaizhan@cuhk.edu.cn

Abstract

The hydrophobic surface of the flavivirus NS1 dimer—comprised primarily of the β-roll domain and the greasy finger loop—is essential for cell surface association and NS1 oligomerization. However, no antibodies targeting this epitope region have been

reported to date. In this study, we employed a pipeline including RFdiffusion, ProteinMPNN, and AlphaFold to design protein binders that target the hydrophobic surface of dengue virus serotype 4 (DENV4) and Zika virus (ZIKV) NS1 dimers. Experimental validation identified five binders for each virus that could be expressed and exhibited specific binding, with equilibrium dissociation constants (K_D) ranging from 45.2 nM to 2.2 μM. Cryo-EM structures of DENV4 NS1 in complex with D4NB4 and D4NB11 and of ZIKV NS1 in complex with ZNB6 confirmed the predicted binding modes. Functional assays demonstrated that these binders inhibit NS1 binding to cell surfaces, highlighting the therapeutic potential of these computationally designed protein binders.

Keywords

flavivirus, NS1, protein binder design, cryo-EM

Introduction

Flaviviruses are enveloped, positive-sense, single-stranded RNA viruses transmitted primarily by mosquitoes, posing a substantial threat to global public health (Pierson and Diamond 2020). Prominent members include Yellow Fever Virus (YFV), Dengue Virus (DENV), Japanese Encephalitis Virus (JEV), West Nile Virus (WNV), and Zika Virus (ZIKV) (Pierson and Diamond 2020). Flavivirus genome encodes three structural proteins (capsid C, envelope E, and precursor membrane prM) and seven non-structural proteins (NS1, NS2A, NS2B, NS3, NS4A, NS4B, and NS5) (Pierson and Diamond 2020). Among these, NS1 is a highly conserved, glycosylated protein with diverse roles in the viral life cycle and pathogenesis (Perera et al. 2024).

The NS1 protein comprises 352 amino acid residues and exists in distinct oligomeric forms that facilitate its diverse roles (Perera et al. 2024). Intracellularly, NS1 forms dimers and contribute to viral RNA synthesis (Welsch et al. 2009; Youn et al. 2012; Scaturro et al. 2015). NS1 is also secreted from infected cells as a hexameric lipoprotein complex (Gutsche et al. 2011). Secreted NS1 plays a critical role in immune evasion by

inhibiting the complement system and can trigger autoimmune responses via molecular mimicry (Cheng et al. 2009; Avirutnan et al. 2010). Furthermore, NS1 binds to host cell surfaces, disrupts the endothelial glycocalyx, and induces endothelial dysfunction and vascular hyperpermeability—processes that contribute to severe disease manifestations such as hemorrhagic fever and shock syndrome (Avirutnan et al. 2007; Modhiran et al. 2015; Puerta-Guardo et al. 2016; Chen et al. 2016). These characteristics, together with its abundance in patient sera during acute infection, render NS1 a valuable diagnostic marker and a promising target for therapeutic interventions and vaccine development against flaviviral diseases.

Crystal structures of the NS1 dimer reveal that NS1 comprises three well-defined domains: an N-terminal β-roll domain, a wing domain, and a C-terminal β-ladder domain, connected by a connector subdomain (Akey et al. 2014; Brown et al. 2016; Xu et al. 2016). Dimerization occurs via intertwining of the β-roll domains and the end-to-end stacking of the β-ladder domains, forming two distinct faces: a hydrophilic outer surface and a hydrophobic inner surface. The hydrophobic surface, formed primarily by the β-roll and an adjacent "greasy finger" loop, mediates association with membranes and high-density lipoprotein particles (Brown et al. 2016; Chew et al. 2024). Cryo-EM structures of NS1 tetramers and hexamers reveal that the hydrophobic surface also plays an essential role in the assembly of NS1 oligomers (Shu et al. 2022; Pan et al. 2024a).

Passive transfer of anti-NS1 antibodies or active immunization with NS1 significantly improves survival rates in mice challenged with lethal doses of DENV, ZIKV, or WNV (Bailey et al. 2019; Biering et al. 2021; Modhiran et al. 2021). Structures of 12 neutralizing antibodies in complex with NS1 have been determined (Edeling et al. 2014; Biering et al. 2021; Modhiran et al. 2021; Shu et al. 2022; Luo et al. 2023; Pan et al. 2024b; Alvin Chew et al. 2024). These antibodies mainly bind to the hydrophilic surface of the NS1 dimer and the distal region of the β-ladder domain. Despite the critical role of the hydrophobic surface in membrane association and hexamer assembly, no neutralizing antibodies targeting this region have been reported. A combination of

factors—pronounced hydrophobicity, conformational flexibility, and convex surface shape—may impede high-affinity antibody binding.

In this study, *de novo* protein binders targeting the hydrophobic surface of DENV4 and ZIKV NS1 dimers were designed using RFdiffusion (Bennett et al. 2025), ProteinMPNN (Dauparas et al. 2022) and AlphaFold (Abramson et al. 2024). Following *in silico* screening, recombinant expression, and purification, we validated five high-affinity binders for DENV4 NS1 and five for ZIKV NS1. The binding modes of three selected binders were further characterized by cryo-EM single particle analysis. Furthermore, these binders effectively inhibited NS1 association with cell surfaces. Our results provide a framework for the *de novo* design of protein binders targeting flavivirus NS1 and offers potential therapeutic candidates for flavivirus infections.

Result

Design and Optimization of Protein Binders Targeting the Hydrophobic Surface of DENV4 and ZIKV NS1 dimer

Dimer Aa from the high-resolution DENV4 NS1 hexamer structure (PDB: 8WBD) was selected as the target for the rational design of protein binders in this study (Fig. 1A, left). Key residues within the β-roll domains of the two constituent monomers—specifically Thr2, Val6, Leu13, and Cys15—were defined as hotspots in RFdiffusion (Fig. 1A, right). The convex topology of the β-roll domain renders it a challenging epitope for creating a continuous binding interface. To overcome this limitation and establish a more extensive interaction network, residue Ser216 on the adjacent β-ladder domain of monomer A was strategically included as an additional hotspot. Similarly, for ZIKV NS1, dimer Aa from the tetrameric structure (PDB: 8WBF) was designated as the design target (Fig. 1B, left). Hotspots specified for RFdiffusion comprised Cys4, Val6, Thr13, and Thr17 in the β-roll domains of both monomers, together with His216 on the β-ladder of monomer A (Fig. 1B, right).

The design began with the *de novo* generation of a protein backbone using RFdiffusion, a diffusion-based generative model that iteratively denoises randomly initialized noise

into a realistic structure (Fig. 1C). Then the amino acid sequence compatible with the designed scaffold was assigned using ProteinMPNN, and the design was finally validated by AlphaFold2, which predicts its folded structure. A design was considered successful if the AlphaFold2-predicted structure closely matches the original RFdiffusion-generated backbone (RMSD < 1 Å), exhibits high predicted local distance difference test scores (pLDDT > 80), and shows low predicted aligned error between the designed protein binder and the target (pAE < 10). Promising candidates were further validated using the AlphaFold3 server, and designs with ipTM > 0.8 were selected for manual inspection.

Certain initial designs featured minimal secondary structures, such as isolated two-α-helix bundles or single-layer β-sheets (Fig. 1D and 1E). These simplified architectures often lack the extensive tertiary packing and buried hydrophobic core necessary for stable folding, limiting recombinant protein expression yield and stability. To address this, an additional computational optimization step was implemented using motif scaffolding in RFdiffusion (Fig. 1D and 1E). This advanced protocol enabled *de novo* design of structured scaffolds around the minimal functional motifs, effectively expanding them into more complex, globular proteins. As shown in Fig. 1D and 1E, the optimized designs exhibit more globular folds and demonstrated improved computational validation scores.

For designed proteins exhibiting suboptimal validation scores, an additional optimization step was performed using the partial diffusion protocol in RFdiffusion (Fig. 1F). By selectively adding noise to the known protein structure and iteratively denoising it, this process effectively samples the conformational space around the initial design, generating diverse set of alternative backbone configurations while preserving core structural motifs. As demonstrated in Fig. 1F, this approach generated design variants with improved *in silico* scores.

Screen and Analysis of Designed Protein Binders

Initially, approximately 12,000 scaffolds and 60,000 sequences were designed for each

target. The pool was further expanded through optimization of suboptimal initial designs via motif scaffolding and partial diffusion. Following structure prediction using AlphaFold2 integrated into the dl_binder_design pipeline and subsequent validation with AlphaFold3, 51 designed protein binders targeting the DENV4 NS1 dimer met the required quality criteria. To ensure structural diversity, we prioritized 12 candidates representing a wide range of molecular weights and three-dimensional topologies (Fig. 2A, Table S1). These 12 candidates were systematically designated D4NB1 through D4NB12 (DENV4 NS1 binder 1 to 12) for clarity. D4NB11 is the most compact binder (71 residues), whereas D4NB2 is the largest (152 residues) (Fig. 2A, Table S1). Seven designs (D4NB1 and D4NB7–12) are dominated by α-helical topology (three to five α-helices), while the remaining five contain β-strands (Fig. 2A). In D4NB2, D4NB4, and D4NB5, the β-sheet surface provides the principal interface with the NS1 dimer, whereas in D4NB3 the β-sheet is excluded from contact (Fig. 2A). D4NB6 presents a mixed interface in which both α-helices and β-strands contribute to binding (Fig. 2A). As shown in Fig. S1A, the majority of the 12 designed protein binders feature a concave binding surface geometrically complementary to the convex β-roll domain of the DENV4 NS1 dimer.

For the ZIKV NS1 dimer, 26 designed protein binders met the required quality criteria. From this pool, seven candidates (designated ZNB1 to ZNB7) were selected for further analysis, with lengths ranging from 78 to 157 amino acid residues (Fig. 2B, Table S1). Structurally, ZNB1, ZNB2, ZNB4, and ZNB5 are α-helical bundle proteins comprising three or four helices, whereas ZNB3, ZNB6, and ZNB7 incorporate β-strands into their topology (Fig. 2B). Overall, the designed proteins exhibit shape complementarity to the β-roll domain of the ZIKV NS1 dimer (Fig. S1B). Notably, ZNB5 represents an exception, primarily interacting with the inner face of the wing domain and the β-ladder domain while making only minor contacts with the β-roll domain (Fig. 2B).

Expression, Purification and Binding Assessment of Designed Protein Binders

The selected protein binders were cloned into a pET21b vector containing a C-terminal

SUMO tag and expressed in *E. coli* BL21(DE3) cells. Among the 12 binders targeting DENV4 NS1, six (D4NB3, D4NB4, D4NB7, D4NB9, D4NB11, and D4NB12) were obtained in soluble form and successfully purified (Fig. S2A–G). Similarly, five of the seven binders targeting ZIKV NS1 (ZNB3, ZNB4, ZNB5, ZNB6, and ZNB7) were expressed and purified (Fig. S3A–F). The binding kinetics and affinities of the purified binders were evaluated by surface plasmon resonance (SPR). As shown in Fig. 3A–E, D4NB3, D4NB4, D4NB7, D4NB9, and D4NB11 bound to DENV4 NS1 with equilibrium dissociation constants (K_D) of 2190, 897, 1500, 681, and 45.2 nM, respectively (Fig. 3F). D4NB12 showed no detectable binding and was excluded from further analysis. All five ZIKV NS1-targeting binders (ZNB3, ZNB4, ZNB5, ZNB6, and ZNB7) also bound to their target (Fig. 3G–K), with K_D values of 477, 458, 433, 374, and 415 nM, respectively (Fig. 3L). These results demonstrate the effectiveness of RFdiffusion and ProteinMPNN for backbone and sequence design and confirm that the ipTM score predicted by AlphaFold3 is a reliable indicator of binding probability.

Cryo-EM Structures of NS1 Complexed with Designed Protein Binders

To elucidate the binding mode of the designed proteins, we selected three designs—D4NB4, D4NB11, and ZNB6—for structural characterization using single-particle cryo-EM. According to the predicted structures, D4NB4 adopts a topology composed of two α-helices and five antiparallel β-strands, with the β-sheet module primarily mediating the interaction with NS1 (Fig. 4A). In contrast, D4NB11 contains three α-helices, of which α1 and α2 are positioned at the binding interface (Fig. 4B). ZNB6 is folded into three parallel β-strands connected by two α-helices, and its binding interface involves β2, α1, α2, and the N-terminal segments of β1 and β3 (Fig. 4C).

Purified protein binders were incubated with the corresponding NS1 proteins, and the resulting DENV4_NS1–D4NB4, DENV4_NS1–D4NB11, and ZIKV_NS1–ZNB6 complexes were isolated by size-exclusion chromatography (Fig. S2H, S2I, and S3G). Cryo-EM grids were prepared, and data were collected. Two-dimensional classification showed that the NS1 dimer constituted the predominant particle class. The structures

of DENV4_NS1–D4NB4, DENV4_NS1–D4NB11 and ZIKV_NS1–ZNB6 were reconstructed at final resolutions of 3.0 Å, 3.0 Å and 3.5 Å, respectively (Fig. S4A, S5A, S6A, and Table S2). Atomic models were built for residues 13–110 of D4NB4, 1–71 of D4NB11, and 2–78 of ZNB6. The overall maps and models are shown in Fig. 4D–F, with focused views of the binder densities provided in Fig. S4B, S5B, and S6B. Although the local resolutions of the protein binders are lower than those of the NS1 dimer (Fig. S4A, S5A, and S6A), secondary-structure elements are clearly traceable, and the side chains at the interface could be roughly defined (Fig. S4B, S5B, and S6B). This moderate local resolution most likely reflects (i) intrinsic flexibility at the NS1-dimer/binder interface and (ii) the inherent flexibility of the β-roll domain, which is required for assembly of NS1 tetramers and hexamers.

To compare the designed and experimentally determined structures of the protein binders, we superposed the binder structures onto the corresponding AlphaFold3-predicted models in ChimeraX and calculated their Cα-RMSD values. The Cα-RMSD values for D4NB4, D4NB11, and ZNB6 were 2.007, 0.513, and 0.745 Å, respectively (Fig. 4G). These results indicate that the designed structures of D4NB11 and ZNB6 align well with the cryo-EM structures, whereas D4NB4 exhibits a larger deviation, particularly in the loop region (Fig. 4G). To further compare the binding poses, we superposed the NS1 β-roll domains from the predicted structures onto those in the cryo-EM structures and calculated the corresponding Cα-RMSD values between the protein binders. For D4NB4 and ZNB6, the Cα-RMSD values were 2.224 and 1.341, respectively—slightly higher than those obtained from superimposing the binders alone (Fig. 4H). This suggests that the binding poses of D4NB4 and ZNB6 remain quite similar to the designs. In contrast, the Cα-RMSD for D4NB11 was 3.536, significantly larger than the value from binder-only superposition, indicating a more substantial difference in its binding pose (Fig. 4H).

The binding interfaces were analyzed in LigPlot^{+} (Fig. S7), revealing notable differences in specific interactions between the cryo-EM structures and the predicted models. In the DENV4_NS1–D4NB4 and DENV4_NS1–D4NB11 complexes,

hydrogen bond interactions predicted *in silico* were not observed in the experimental structures (Fig. S7A and S7B). For ZIKV_NS1–ZNB6, the hydrogen bonding network also differed from the prediction (Fig. S7C). Interestingly, the conformation of the "greasy finger" loop in monomer 1 of the ZIKV NS1 dimer differed between the experimental and predicted structures (Fig. 4I). As shown in Fig. 4J, the cryo-EM structure of ZIKV_NS1–ZNB6 reveals that this loop adopts a conformation similar to that observed in the cryo-EM structure of the ZIKV NS1 tetramer (PDB: 8WBF), which served as the input for RFdiffusion in this study. In contrast, the AlphaFold3-predicted structure exhibits a loop conformation more closely resembling that of the ZIKV NS1 dimer crystal structure (PDB: 5K6K) (Fig. 4K). These comparisons suggest that although AlphaFold3 predictions effectively indicate the potential binding capability of the designed proteins to their targets, the precise binding pose and specific interfacial interactions may deviate from those observed in experimental structures.

Inhibition of NS1 Binding to Cell Surface by Designed Protein Binders

To assess the potential of the designed binders to inhibit NS1 function, we performed cell-surface NS1 binding inhibition assays. D4NB4 and D4NB11 inhibited the binding of DENV4 NS1 to the cell surface with IC_{50} values of 3.09 and 6.16 μM, respectively (Fig. 5A, 5C, and S8). Their potency was lower than that of the monoclonal antibody 2B7 (IC_{50} = 0.02 μM) (Fig. 5A, 5C, and S8), likely due to the designed binders' lower affinity compared to the reported high affinity of 2B7 (4.8 ± 3.1 nM for DENV2 NS1) (Modhiran et al. 2021). However, both D4NB4 and D4NB11 were slightly more potent than peptide 4F (IC_{50}= 9.56 μM) (Fig. 5A, 5C, and S8), an ApoA1-mimetic peptide that blocks flavivirus NS1-triggered endothelial dysfunction (Carneiro et al. 2024). For ZIKV NS1, the designed binder ZNB6 inhibited cell-surface binding with an IC_{50} of 0.45 μM (Fig. 5B, 5C, and S9), suggesting a lower potency compared with antibody 2B7 (0.02 μM) and peptide 4F (0.11 μM) (Fig. 5B, 5C, and S9). These results demonstrate that the designed protein binders can modulate NS1 function by blocking its attachment to cell surfaces, revealing their potential as therapeutic candidates.

Discussion

The β-roll and the adjacent greasy finger loop form the core of the hydrophobic surface of flavivirus NS1 dimer, which not only mediates NS1 association with intracellular and cell-surface membranes but also constitutes a critical interface for NS1 oligomerization into the secreted hexameric lipoprotein complex. Thus, the β-roll represents a strategic vulnerability for therapeutic intervention. In this study, our designs were explicitly targeted to this structurally conserved and functionally indispensable element of NS1 dimer.

Despite challenges posed by the pronounced hydrophobicity, conformational flexibility, and convex surface shape of the β-roll—which complicate *de novo* protein binder design, our integrated computational and experimental strategy successfully generated functional protein binders. We employed a large-scale design strategy involving numerous scaffolds and sequences, coupled with iterative *in silico* optimization and experimental validation. This strategy yielded 51 and 26 *de novo* designed protein binders against DENV4 NS1 and ZIKV NS1, respectively. From these pools, we selected 12 DENV4 and 7 ZIKV NS1 binders, representing a diverse array of secondary structures, for expression and purification. Five binders for each target were confirmed by surface plasmon resonance. Furthermore, we elucidated the precise binding mechanisms for three lead candidates—D4NB4, D4NB11, and ZNB6—by determining high-resolution cryo-EM structures of their complex with NS1. These structures confirmed that the binders engage the β-roll as designed. By blocking the hydrophobic face required for both membrane interaction and higher-order assembly, these binders may effectively antagonize two essential steps in NS1-mediated pathogenicity. Further functional assays demonstrated that these *de novo* designed proteins could inhibit NS1 cell-surface association. One limitation of this study is that the binding affinities of current designs remain relatively modest, failing to reach the nanomolar range, which may explain why the designed protein binders exhibited lower potency compared with the high-affinity antibody 2B7. This may be related to the inherent constraints of the β-

roll domain. The absence of deep pockets and sufficient polar interactions may limit the formation of high-affinity contacts. Further affinity maturation and the development of broad-spectrum binders capable of recognizing NS1 across flaviviruses, though highly challenging, could yield more valuable therapeutic tools.

Our findings also demonstrate that predictions generated by AlphaFold3 serve as reliable indicators of the binding capability of designed proteins to their intended targets. However, in certain cases, the predicted binding pose and atomic-level interaction networks differ from those observed in experimentally determined structures. This highlights remaining areas for improvement in computational protein structure prediction. Moreover, without reliable indicators of binding affinity, the current selection of candidate designs for experimental testing remains largely empirical. Such tools would greatly streamline the protein binder design process by enabling more robust *in silico* screening and optimization, thereby substantially reducing the experimental workload required for validation.

Acknowledgements

We thank the Kobilka Cryo-EM Center at the Chinese University of Hong Kong, Shenzhen, for supporting EM data collection. We thank Xuezhen Lin from the Sample Preparation and Analysis Core Facility of the Bio-Tech Center at Shenzhen Medical Academy of Research and Translation (SMART) for performing SPR analysis.

Funding

This work was supported by the National Natural Science Foundation of China, Youth Science Fund (32501293 to H.J), and Shenzhen Medical Research Fund, Youth Program (A2403008 to H.J.). This work was also supported by the National Natural Science Foundation of China (32471254 and 82430027 to H.H, and 52388101 to J.X), and Shenzhen Science and Technology Innovation Committee (JCYJ20240813113600001 to H.H.). This work was also supported by the Kobilka Institute of Innovative Drug Discovery and Presidential Fellowship and University

Development Fund at the Chinese University of Hong Kong, Shenzhen (H.H. and H.J.).

Author Contributions

Conceptualization: H.J, H.H; Investigation: H.J, Q.P, G.Z, J.Y, W.Z, S.Z, J.X, W.Z; Visualization: Q.P. Funding acquisition: H.J, H.H, J.X; Supervision: H.J, H.H; Writing: H.J, H.H.

Consent to participate

All authors give their consent to participate.

Consent for Publication

All authors approve the publication of this manuscript.

Conflict of interests

The authors declare no competing interests.

Data availability

The cryo-EM maps of DENV4_NS1–D4NB4, DENV4_NS1–D4NB11 and ZIKV_NS1–ZNB6 complexes have been deposited in the EMDB under accession codes EMD-67018, EMD-67019, and EMD-67020, respectively. The atomic models of DENV4_NS1–D4NB4, DENV4_NS1–D4NB11 and ZIKV_NS1–ZNB6 complexes have been deposited in the PDB under accession codes 9XMA, 9XMB, and 9XMC respectively.

References

Abramson J, Adler J, Dunger J, et al (2024) Accurate structure prediction of biomolecular interactions with AlphaFold 3. Nature 630:493–500. https://doi.org/10.1038/s41586-024-07487-w

Afonine PV, Poon BK, Read RJ, et al (2018) Real-space refinement in *PHENIX* for cryo-EM and crystallography. Acta Crystallogr Sect Struct Biol 74:531–544. https://doi.org/10.1107/S2059798318006551

Akey DL, Brown WC, Dutta S, et al (2014) Flavivirus NS1 Structures Reveal Surfaces for Associations with Membranes and the Immune System. Science 343:881–885. https://doi.org/10.1126/science.1247749

Alvin Chew BL, Pan Q, Hu H, Luo D (2024) Structural biology of flavivirus NS1 protein and its antibody complexes. Antiviral Res 227:105915. https://doi.org/10.1016/j.antiviral.2024.105915

Avirutnan P, Fuchs A, Hauhart RE, et al (2010) Antagonism of the complement component C4 by flavivirus nonstructural protein NS1. J Exp Med 207:793–806. https://doi.org/10.1084/jem.20092545

Avirutnan P, Zhang L, Punyadee N, et al (2007) Secreted NS1 of dengue virus attaches to the surface of cells via interactions with heparan sulfate and chondroitin sulfate E. PLoS Pathog 3:e183. https://doi.org/10.1371/journal.ppat.0030183

Bailey MJ, Broecker F, Duehr J, et al (2019) Antibodies elicited by an NS1-based vaccine protect mice against zika virus. mBio 10:e02861-18. https://doi.org/10.1128/mBio.02861-18

Bennett NR, Watson JL, Ragotte RJ, et al (2025) Atomically accurate de novo design of antibodies with RFdiffusion. Nature 1–11. https://doi.org/10.1038/s41586-025-09721-5

Biering SB, Akey DL, Wong MP, et al (2021) Structural basis for antibody inhibition of flavivirus NS1–triggered endothelial dysfunction. Science 371:194–200. https://doi.org/10.1126/science.abc0476

Brown WC, Akey DL, Konwerski JR, et al (2016) Extended surface for membrane association in zika virus NS1 structure. Nat Struct Mol Biol 23:865–867. https://doi.org/10.1038/nsmb.3268

Carneiro PH, Jimenez-Posada EV, Lopes E, et al (2024) The ApoA1-mimetic peptide 4F blocks flavivirus NS1-triggered endothelial dysfunction and protects against lethal dengue virus challenge. Antiviral Res 231:106002. https://doi.org/10.1016/j.antiviral.2024.106002

Chen H-R, Chuang Y-C, Lin Y-S, et al (2016) Dengue virus nonstructural protein 1 induces vascular leakage through macrophage migration inhibitory factor and autophagy. PLoS Negl Trop Dis 10:e0004828. https://doi.org/10.1371/journal.pntd.0004828

Chen VB, Arendall WB, Headd JJ, et al (2010) *MolProbity*: all-atom structure validation for macromolecular crystallography. Acta Crystallogr D Biol Crystallogr 66:12–21. https://doi.org/10.1107/S0907444909042073

Cheng H-J, Lei H-Y, Lin C-F, et al (2009) Anti-dengue virus nonstructural protein 1

antibodies recognize protein disulfide isomerase on platelets and inhibit platelet aggregation. Mol Immunol 47:398–406. https://doi.org/10.1016/j.molimm.2009.08.033

Chew BLA, Ngoh ANQ, Phoo WW, et al (2024) Secreted dengue virus NS1 from infection is predominantly dimeric and in complex with high-density lipoprotein. eLife 12:RP90762. https://doi.org/10.7554/eLife.90762

Dang B, Mravic M, Hu H, et al (2019) SNAC-tag for sequence-specific chemical protein cleavage. Nat Methods 16:319–322. https://doi.org/10.1038/s41592-019-0357-3

Dauparas J, Anishchenko I, Bennett N, et al (2022) Robust deep learning–based protein sequence design using ProteinMPNN. Science 378:49–56. https://doi.org/10.1126/science.add2187

Edeling MA, Diamond MS, Fremont DH (2014) Structural basis of Flavivirus NS1 assembly and antibody recognition. Proc Natl Acad Sci 111:4285–4290. https://doi.org/10.1073/pnas.1322036111

Gutsche I, Coulibaly F, Voss JE, et al (2011) Secreted dengue virus nonstructural protein NS1 is an atypical barrel-shaped high-density lipoprotein. Proc Natl Acad Sci 108:8003–8008. https://doi.org/10.1073/pnas.1017338108

Jakobi AJ, Wilmanns M, Sachse C (2017) Model-based local density sharpening of cryo-EM maps. eLife 6:e27131. https://doi.org/10.7554/eLife.27131

Liebschner D, Afonine PV, Baker ML, et al (2019) Macromolecular structure determination using X-rays, neutrons and electrons: Recent developments in phenix. Acta Crystallogr Sect Struct Biol 75:861–877. https://doi.org/10.1107/S2059798319011471

Luo D, Chew BLA, Ngoh AQ, et al (2023) Structural basis of Zika virus NS1 multimerization and human antibody recognition

Modhiran N, Song H, Liu L, et al (2021) A broadly protective antibody that targets the flavivirus NS1 protein. Science 371:190–194. https://doi.org/10.1126/science.abb9425

Modhiran N, Watterson D, Muller DA, et al (2015) Dengue virus NS1 protein activates cells via toll-like receptor 4 and disrupts endothelial cell monolayer integrity. Sci Transl Med 7:. https://doi.org/10.1126/scitranslmed.aaa3863

Pan Q, Jiao H, Zhang W, et al (2024a) The step-by-step assembly mechanism of secreted flavivirus NS1 tetramer and hexamer captured at atomic resolution. Sci Adv 10:eadm8275. https://doi.org/10.1126/sciadv.adm8275

Pan Q, Xing X, Yu J, et al (2024b) Structural insights into the distinct protective mechanisms of human antibodies targeting ZIKV NS1. hLife. https://doi.org/10.1016/j.hlife.2024.05.003

Perera DR, Ranadeva ND, Sirisena K, Wijesinghe KJ (2024) Roles of NS1 Protein in Flavivirus Pathogenesis. ACS Infect Dis 10:20–56. https://doi.org/10.1021/acsinfecdis.3c00566

Pettersen EF, Goddard TD, Huang CC, et al (2021) UCSF ChimeraX: Structure visualization for researchers, educators, and developers. Protein Sci 30:70–82. https://doi.org/10.1002/pro.3943

Pierson TC, Diamond MS (2020) The continued threat of emerging flaviviruses. Nat Microbiol 5:796–812. https://doi.org/10.1038/s41564-020-0714-0

Puerta-Guardo H, Glasner DR, Harris E (2016) Dengue virus NS1 disrupts the endothelial glycocalyx, leading to hyperpermeability. PLoS Pathog 12:e1005738. https://doi.org/10.1371/journal.ppat.1005738

Punjani A, Rubinstein JL, Fleet DJ, Brubaker MA (2017) cryoSPARC: algorithms for rapid unsupervised cryo-EM structure determination. Nat Methods 14:290–296. https://doi.org/10.1038/nmeth.4169

Scaturro P, Cortese M, Chatel-Chaix L, et al (2015) Dengue Virus Non-structural Protein 1 Modulates Infectious Particle Production via Interaction with the Structural Proteins. PLOS Pathog 11:e1005277. https://doi.org/10.1371/journal.ppat.1005277

Shu B, Ooi JSG, Tan AWK, et al (2022) CryoEM structures of the multimeric secreted NS1, a major factor for dengue hemorrhagic fever. Nat Commun 13:6756. https://doi.org/10.1038/s41467-022-34415-1

Terwilliger TC, Sobolev OV, Afonine PV, Adams PD (2018) Automated map sharpening by maximization of detail and connectivity. Acta Crystallogr Sect Struct Biol 74:545–559. https://doi.org/10.1107/S2059798318004655

Welsch S, Miller S, Romero-Brey I, et al (2009) Composition and three-dimensional architecture of the dengue virus replication and assembly sites. Cell Host Microbe 5:365–375. https://doi.org/10.1016/j.chom.2009.03.007

Xu X, Song H, Qi J, et al (2016) Contribution of intertwined loop to membrane association revealed by zika virus full-length NS1 structure. EMBO J 35:2170–2178. https://doi.org/10.15252/embj.201695290

Youn S, Li T, McCune BT, et al (2012) Evidence for a genetic and physical interaction between nonstructural proteins NS1 and NS4B that modulates replication of west nile virus. J Virol 86:7360–7371. https://doi.org/10.1128/JVI.00157-12

Zheng SQ, Palovcak E, Armache JP, et al (2017) MotionCor2: anisotropic correction of beam-induced motion for improved cryo-electron microscopy. Nat Methods 14:331–332. https://doi.org/10.1038/nmeth.4193

Zhu J, Zhang Q, Zhang H, et al (2023) A minority of final stacks yields superior amplitude in single-particle cryo-EM. Nat Commun 14:1–11. https://doi.org/10.1038/s41467-023-43555-x

Methods

Design of Protein Binders Using RFdiffusion, ProteinMPNN, and AlphaFold

The dimer Aa from the DENV4 NS1 hexamer structure (PDB: 8WBD) was selected as the target, with residues Thr2, Val6, Leu13, Cys15, and Ser216 designated as hotspots. For ZIKV NS1, dimer Aa from the tetrameric structure (PDB: 8WBF) was selected as the target, with Cys4, Val6, Thr13, Thr17, and His216 designated as hotspots. Scaffold length was restricted to 40–100 amino acids. To enhance topological diversity, the Complex_beta_ckpt.pt model was employed to generate β-sheet-containing scaffolds. Additionally, denoiser parameters (denoiser.noise_scale_ca = 0.5; denoiser.noise_scale_frame = 0.5) were adjusted to further increase diversity. Approximately 12,000 scaffolds were generated in total.

Binder scaffold PDB files generated by RFdiffusion were converted to silent files using Rosetta's SilentFile utilities. Sequence design was subsequently performed using ProteinMPNN within the dl_binder_design software package. For each scaffold, four sequences were generated with fast_relax_cycles = 0, and one additional sequence was produced with fast_relax_cycles = 1.

Protein binder structures were predicted using AlphaFold2 implemented in the dl_binder_design software package. Initial selection was based on thresholds of pAE < 10, RMSD < 1 Å, and pLDDT > 80. Selected binders were subsequently validated using the online AlphaFold3 server. Those achieving an ipTM score > 0.8 were retained for further analysis.

Optimization of Protein Binders through Motif Scaffolding and Partial Diffusion

To enhance the stability of binders containing only two α-helices and a single β-sheet layer–which often exhibit poor expression–we employed motif scaffolding. Specifically, we appended 0-50 residues to either the N- or C-terminus of the designed binders. 200 optimized scaffolds were generated with denoiser.noise_scale_ca = 0 and denoiser.noise_scale_frame = 0. All scaffolds underwent sequence generation using ProteinMPNN followed by structural validation with AlphaFold as previously described.

Binders with suboptimal scores received additional optimization through partial diffusion (diffuser.partial_T = 10 or 20). For each partial_T setting, 100 designs were generated. These optimized scaffolds similarly progressed through ProteinMPNN sequence generation and AlphaFold structure prediction using our established pipeline.

Expression and Purification of Protein Binders

For binders lacking an N-terminal methionine, an MSG tripeptide was fused to their N-terminus. A SUMO protein tag, preceded by a SNAC cleavage site (GSHHW) (Dang et al. 2019), was fused to the C-terminus. The optimized binder genes were synthesized and cloned into the pET21b vector using NdeI and BamHI restriction sites. Proteins were expressed in *E. coli* BL21(DE3) cells cultured in Terrific Broth supplemented with 50 μg/mL ampicillin. Expression was induced with 0.5 mM IPTG when the OD_{600} reached 1.0 and continued overnight at 16°C.

For purification of the expressed recombinant protein binders, cell pellets harvested by centrifugation were resuspended in lysis buffer (20 mM HEPES-Na, pH 8.0, 300 mM NaCl, 10 mM imidazole). Following cell lysis via high-pressure homogenization, the lysate was centrifuged at 40,000 × g for 30 min. The clarified supernatant was subjected to Ni-NTA affinity chromatography, with stepwise elution using buffers containing 20 mM HEPES-Na, pH 7.5, 150 mM NaCl, 10% glycerol, and either 20, 50, or 300 mM imidazole. The 300-mM imidazole elution fraction was pooled, concentrated using a 10-kDa MWCO centrifugal concentrator, and further purified by size-exclusion chromatography on a Superdex 200 Increase 10/300 GL column (Cytiva) equilibrated

with 25 mM HEPES-Na, pH 7.5, 150 mM NaCl.

DENV4 and ZIKV NS1 proteins were expressed and purified according to a previous protocol (Pan et al. 2024a).

Assessment of Binding Affinity via SPR

DENV4 and ZIKV NS1 dimers were immobilized on a CM5 sensor chip via amine coupling (NHS/EDC) using a Biacore 8K+ instrument (Cytiva). All SPR experiments were performed at 25 ℃. Serial dilutions of each purified binder were injected over the sensor surface at the following concentration ranges: 0.3704–10 μM for D4NB3, 0.3125–10 μM for D4NB4 and D4NB7; 0.625–5 μM for D4NB9; 1.25–20 μM for D4NB11; and 0.0137–3.33 μM for ZNB3, ZNB4, ZNB5, ZNB6, and ZNB7. The binding cycle consisted of a 120-s association phase and a 180-s dissociation phase, with a constant flow rate of 30 μL/min in running buffer (20 mM HEPES-Na, pH 7.5, 150 mM NaCl, 0.05% Tween-20). The sensor surface was regenerated after each cycle with 10 mM glycine-HCl, pH 2.0, injected for 30 s at 30 μL/min. Sensorgram data were fitted to a 1:1 binding model using Biacore Insight Evaluation Software 5.0. Figures were prepared in GraphPad Prism.

Preparation of Cryo-EM Samples and Data Collection

NS1 and protein binders were incubated on ice for 0.5 h at a molar ratio of 1:2. Then the NS1–binder complex was purified through size-exclusion chromatography on a Superdex200 Increase Column in a buffer containing 20 mM HEPES-Na, pH=7.5, and 150 mM NaCl. The complex fractions were collected and concentrated to around 1 mg/mL.

For cryo-EM grid preparation, 3.5 μL of purified NS1-binder complex was applied to amorphous alloy film (CryoMatrix Au300-R12/13, Zhenjiang Lehua Electronic Technology Co. Ltd.). The grids were blotted for 3.5 s at 4°C with 100% humidity using Vitrobot IV (Thermo Fisher Scientific), frozen in liquid ethane, and stored in liquid nitrogen.

The grids were imaged using a 300 kV Titan Krios G3i equipped with a Gatan K3 Summit detector. The movie stacks with 50 frames were automatically collected using SerialEM software at a nominal magnification of 105,000×, corresponding to a pixel size of 0.85 Å. The defocus ranges from −1.2 to −1.8 μm. Each movie stack was exposed in the counted-Nanoprobe mode for 2.5 − 3.0 s, and the total dose rate was approximately 48.42 − 49.40 $e^-/Å^2$.

Processing of Cryo-EM Data and Structure Reconstruction

For the DENV4_NS1–D4NB4 and DENV4_NS1–D4NB11 complexes, 3,393 and 6,111 movies were collected, respectively. Beam-induced motion was corrected in RELION 5.0 using MotionCorr2 (Zheng et al. 2017), and the resulting micrographs were imported into CryoSPARC (Punjani et al. 2017), where CTF parameters were estimated with PatchCTF. Particle picking with the Template Picker yielded 4,952,298 and 9,362,396 particles, respectively, which were extracted at a pixel size of 1.7 Å. Following 2D classification, ab initio reconstruction, and heterogeneous refinement, 453,287 and 737,723 particles were retained and subsequently re-extracted in RELION at a pixel size of 0.85 Å. Two rounds of 3D classification without alignment were performed, resulting in 132,236 and 106,756 particles selected for CTF refinement, particle polishing, and 3D auto-refinement. This process generated 3.0 Å resolution maps for both complexes. Finally, map intensities were locally scaled with LocScale (Jakobi et al. 2017) and sharpened with Phenix AutoSharpen (Terwilliger et al. 2018; Liebschner et al. 2019) to improve interpretability.

For the ZIKV_NS1–ZNB6 complex, 1,935 movies were collected and imported into CryoSPARC. Motion correction was carried out using Patch Motion Correction, followed by CTF estimation with PatchCTF. Particle picking and extraction yielded 2,040,256 particles at a pixel size of 1.7 Å. Subsequent 2D classification, ab initio reconstruction, and heterogeneous refinement reduced the dataset to 167,240 particles, which were then re-extracted at a pixel size of 0.85 Å. After reference-based

motion correction, particles were imported into RELION 5.0 for 3D auto-refinement. Particle sieving was then performed in CryoSIEVE (Zhu et al. 2023), yielding 107,034 particles that were used for the final 3D auto-refinement, producing a 3.5 Å resolution map. Map intensities were further processed using LocScale for local scaling and Phenix AutoSharpen for sharpening, thereby enhancing map interpretability.

Model Building and Refinement

The AlphaFold3-predicted NS1–binder structure was docked into the cryo-EM density map using ChimeraX (Pettersen et al. 2021). Rigid-body refinement, morphing, and simulated annealing were initially performed in Phenix Real_Space_Refine (Afonine et al. 2018), followed by iterative cycles of refinement in Phenix Real_Space_Refine using default parameters with secondary structure restraints. Manual model adjustments were carried out in Coot during these iterative cycles. The geometries of the refined models were assessed using MolProbity (Chen et al. 2010). Structural figures were generated in ChimeraX.

Cell-Surface NS1 Binding Inhibition Assay

Two types of target cells were used for inhibition assays: human brain microvascular endothelial cells (HBMECs) were used for DENV4 NS1, and human umbilical vein endothelial cells (HUVECs) were used for ZIKV NS1. HBMECs and HUVECs were cultured at 37 ℃ and 5% CO_2 for 24 h, and then detached from the culture flask using 0.25% trypsin-EDTA (GIBCO, USA). The cells were fixed at 4 ℃ for 20 mins using BD Cytofix/Cytoperm (BD, USA) and resuspended in a binding solution (4mM EDTA, 1× PBS, 5% FBS) for subsequent use. DENV4 NS1 (10 μg/mL) and ZIKV NS1 (5 μg/mL) were incubated with gradient-diluted protein binders or antibodies at 37 ℃ for 1 h. Protein binder D4NB4 and D4NB11 targeted DENV4 NS1, ZNB6 targeted ZIKV NS1, peptide 4F and monoclonal antibody 2B7 targeted both NS1 types. Meanwhile, gradient-diluted SUMO proteins were set as negative controls. After the incubation, 2

604 $\times 10^5$ fixed corresponding target cells were added and allowed to bind at 4 ℃ for 1 h.
605 Following two washes with pre-cooled PBS, the cells were incubated with either FITC-
606 labeled Strep-tag II monoclonal antibodies (Proteintech, China) diluted 1:100 or FITC-
607 labeled sheep anti-mouse IgG (Sangon, China) diluted 1:500 at 4 ℃ for 1 h. After
608 another two washes with cold PBS, the cells were resuspended in the binding buffer.
609 Detection was carried out using a NovoCyte™ flow cytometer (Agilent, USA). The
610 data were analyzed with NovoExpress v1.6.2 software and processed using GraphPad
611 Prism v9.5.1 software. Inhibition curves depicting the binding of NS1 to target cells
612 were generated using the nonlinear variable slope (four-parameter) inhibition curve
613 fitting method in GraphPad Prism.

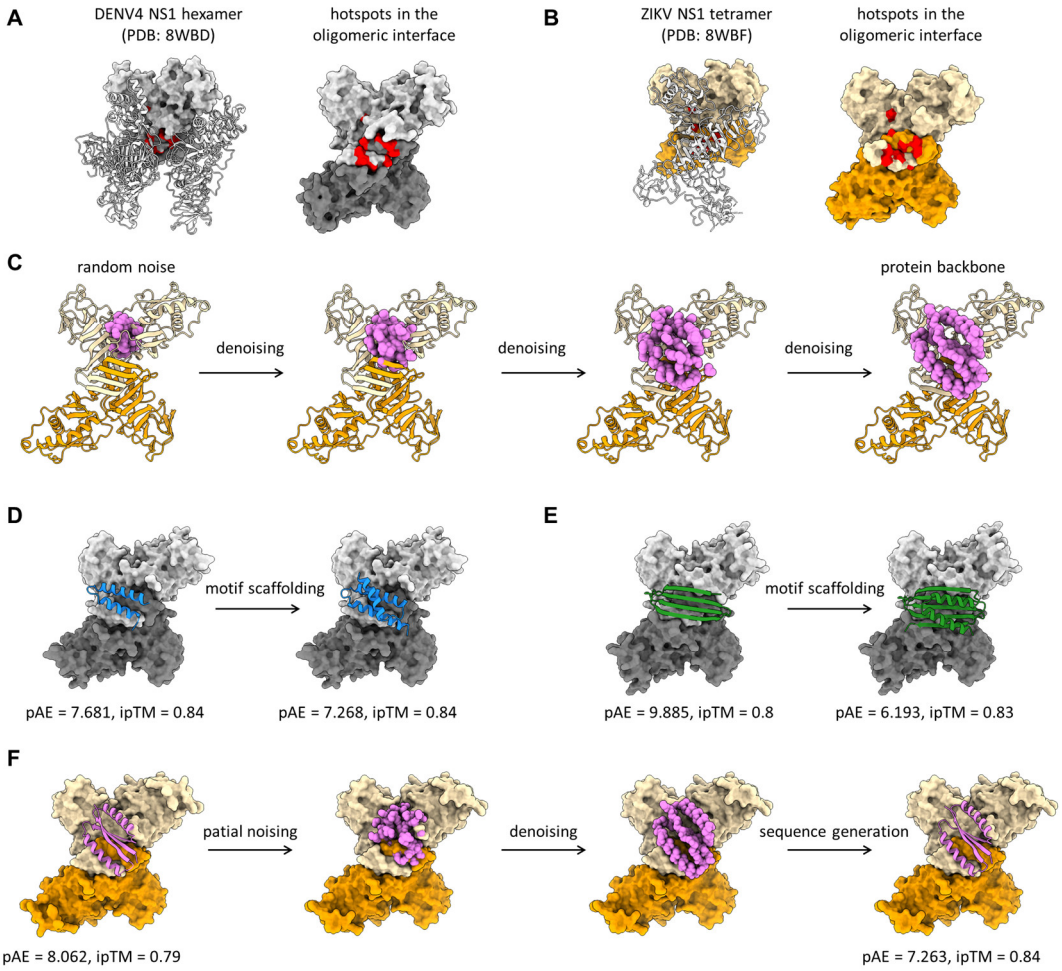

Figure 1. Computational design and optimization of *de novo* protein binders targeting the hydrophobic surface of the NS1 dimer.

(A) Target selection for DENV4 NS1. (*Left*) Structure of the DENV4 NS1 hexamer (PDB: 8WBD), with the Aa dimer shown as surface and the Bb and Cc dimer shown as cartoon. (*Right*) The surface model of Aa dimer (light gray and dark gray) with hotspots (Thr2, Val6, Leu13, and Cys15 from both monomers, and Ser216 from monomer A) highlighted in red.

(B) Target selection for ZIKV NS1. (*Left*) Structure of the ZIKV NS1 tetramer (PDB: 8WBF), with the Aa dimer shown as surface and the Bb dimer shown as cartoon. (*Right*) The surface model of Aa dimer (wheat and orange) with the hotspots (Cys4, Val6, Thr13, Thr17 from both monomers, and His216 from monomer A) highlighted in red.

(C) *De novo* backbone generation with RFdiffusion. The computational pipeline generated initial protein binder backbones (spheres, violet) designed to complement the

hydrophobic target surface on the ZIKV NS1 Aa dimer (cartoon, wheat and orange).

(D, E) Backbone optimization through motif scaffolding. The two-α-helix bundle design (blue, cartoon) and single-layer β-sheet design (green, cartoon) were expanded into more complex, globular proteins using the motif scaffolding protocol in RFdiffusion. The target DENV4 NS1 dimer is shown as surface (light gray and dark gray).

(F) Backbone optimization through partial diffusion. Designs with suboptimal validation scores (violet, spheres or cartoon) underwent further optimization via partial diffusion in RFdiffusion. The target ZIKV NS1 dimer is shown as surface (wheat and orange)

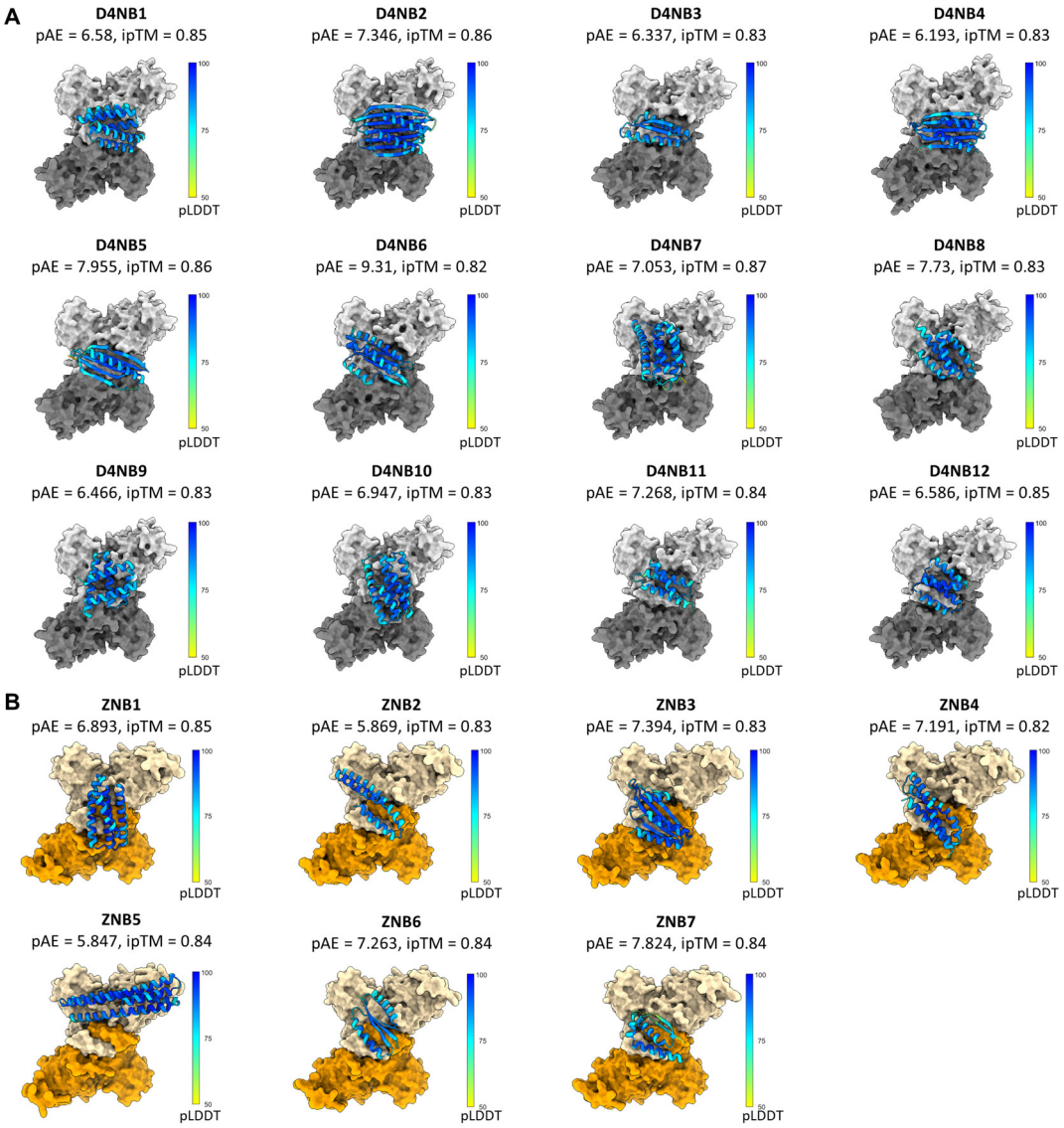

Figure 2. Selected protein binders for protein expression.

(A) Selected protein binders (cartoon, colored by pLDDT values) targeting the hydrophobic surface of the DENV4 NS1 dimer (surface, light gray and dark gray).

(B) Selected protein binders (cartoon, colored by pLDDT values) targeting the hydrophobic surface of the ZIKV NS1 dimer (surface, wheat and orange). In A and B, pAE values predicted by AlphaFold2, ipTM values predicted by AlphaFold3, and the pLDDT color scale are presented.

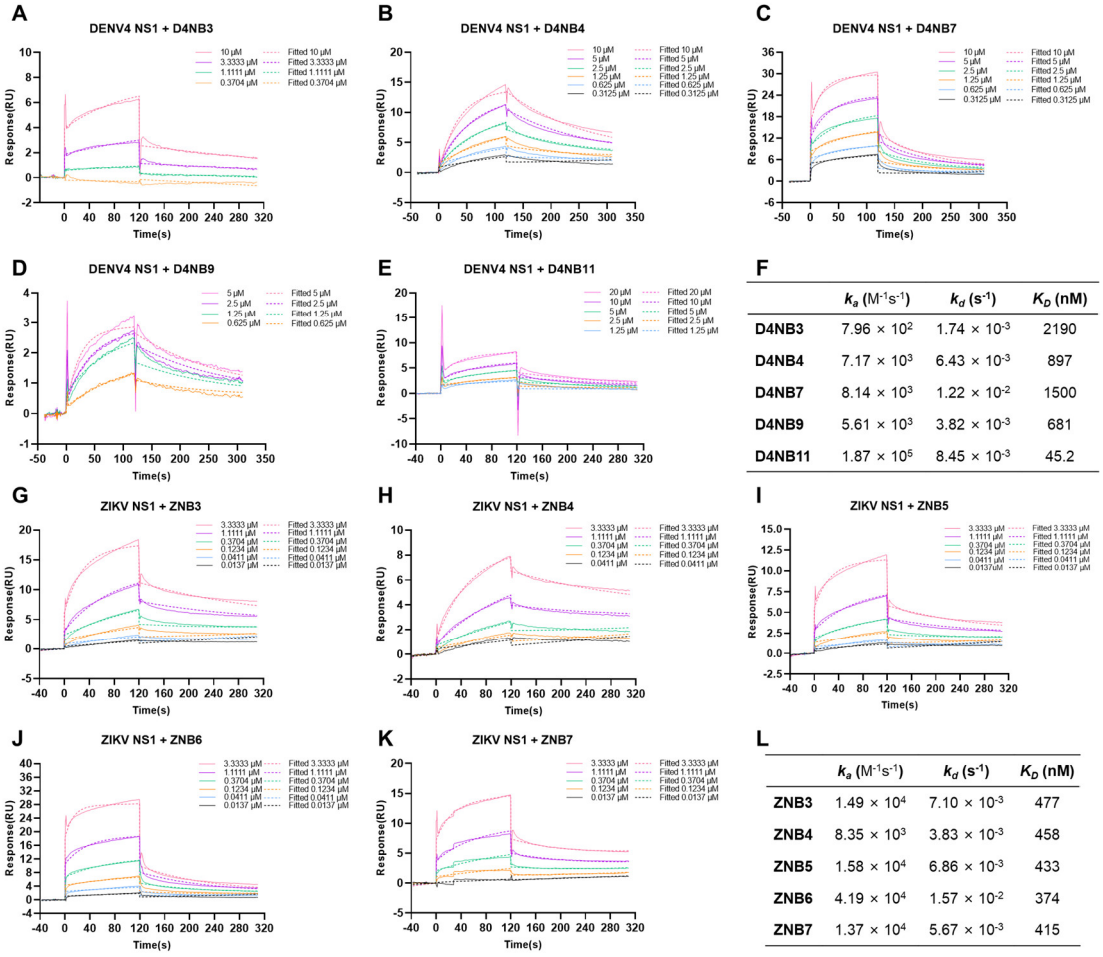

F

	k_a ($M^{-1}s^{-1}$)	k_d (s^{-1})	K_D (nM)
D4NB3	7.96×10^2	1.74×10^{-3}	2190
D4NB4	7.17×10^3	6.43×10^{-3}	897
D4NB7	8.14×10^3	1.22×10^{-2}	1500
D4NB9	5.61×10^3	3.82×10^{-3}	681
D4NB11	1.87×10^5	8.45×10^{-3}	45.2

L

	k_a ($M^{-1}s^{-1}$)	k_d (s^{-1})	K_D (nM)
ZNB3	1.49×10^4	7.10×10^{-3}	477
ZNB4	8.35×10^3	3.83×10^{-3}	458
ZNB5	1.58×10^4	6.86×10^{-3}	433
ZNB6	4.19×10^4	1.57×10^{-2}	374
ZNB7	1.37×10^4	5.67×10^{-3}	415

Figure 3. Binding kinetics of the designed protein binders.

(A–E) SPR sensorgrams showing the binding of designed binders D4NB3 (A), D4NB4 (B), D4NB7 (C), D4NB9 (D), and D4NB11 (E) to DENV4 NS1.

(F) Summary of the kinetic and affinity parameters derived from SPR for the binders targeting DENV4 NS1.

(G–K) SPR sensorgrams showing the binding of designed binders ZNB3 (G), ZNB4 (H), ZNB5 (I), ZNB6 (J), and ZNB7 (K) to ZIKV NS1.

(L) Summary of kinetic and affinity parameters derived from SPR for the binders targeting ZIKV NS1. In F and L, values for the equilibrium dissociation constant (K_D), association rate constant (k_a), and dissociation rate constant (k_d) are shown. Data from a representative experiment were fitted to a 1:1 binding model. N.D., not detected.

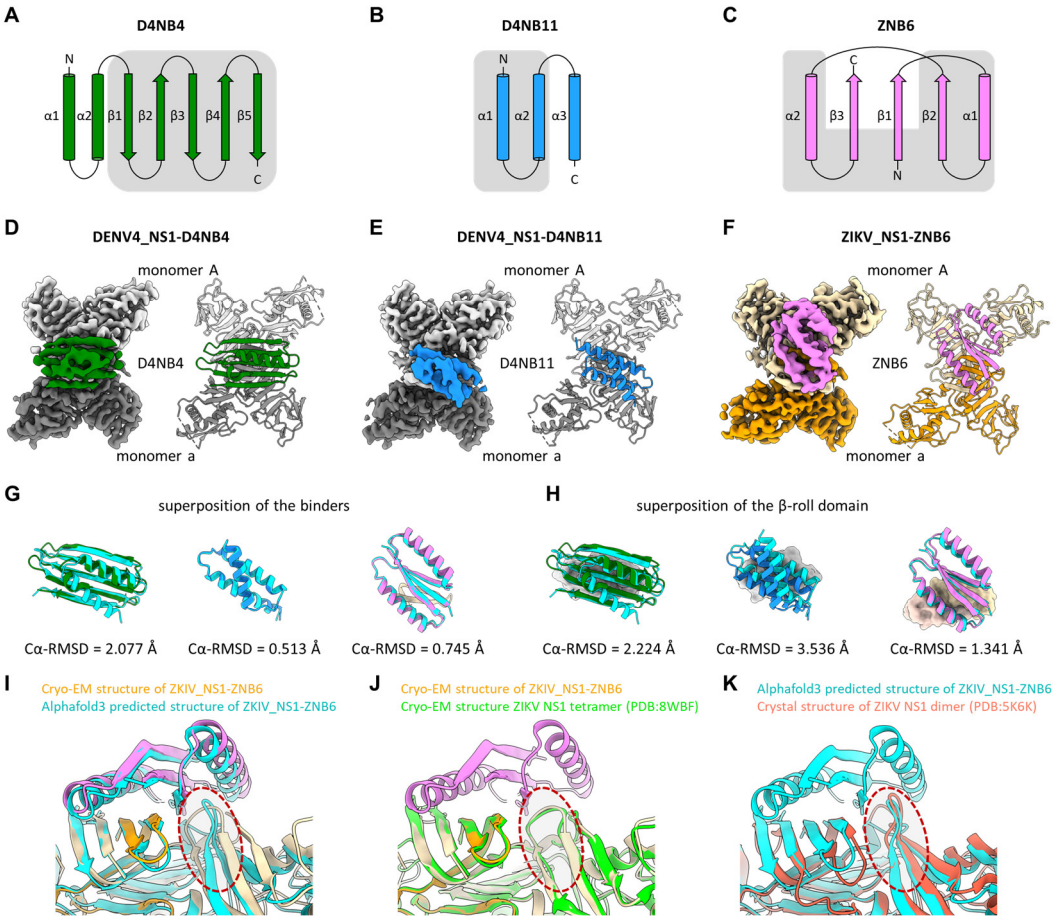

Figure 4. Cryo-EM structures of DENV4_NS1–D4NB4, DENV4_NS1–D4NB11, and ZIKV_NS1–ZNB6.

(A–C) Secondary structure topology diagrams of designed binders D4NB4 (A), D4NB11 (B), and ZNB6 (C). β-strands are shown as arrows and α-helices as cylinders. Regions predicted to interact with NS1 are highlighted with gray backgrounds.

(D–F) Cryo-EM maps (surface) and atomic models (cartoon) for the DENV4_NS1–D4NB4 (D), DENV4_NS1–D4NB11 (E), and ZIKV_NS1–ZNB6 (F) complexes.

(G) Superposition of the experimentally determined binder structures (cartoon) onto their AlphaFold3 models (cartoon).

(H) Comparison of binder binding poses after structural superposition based on the NS1 β-roll domain. The binders and the NS1 β-roll domains from the cryo-EM structures are displayed as cartoon and surface, respectively. AlphaFold3-predicted models are shown as cartoon and colored cyan.

(I) Comparison of the "greasy finger" loop conformation in the ZIKV_NS1–ZNB6

cryo-EM structure (cartoon) with that in the AlphaFold3 model (cartoon, cyan).

(J) Comparison of the "greasy finger" loop conformation in the ZIKV_NS1–ZNB6 cryo-EM structure (cartoon) with that in the ZIKV NS1 tetramer (PDB: 8WBF, cartoon, lime).

(K) Comparison of the "greasy finger" loop conformation in the AlphaFold3-predicted ZIKV_NS1–ZNB6 structure (cartoon, cyan) with that in the ZIKV NS1 dimer crystal structure (PDB: 5K6K, cartoon, tomato). In all panels (A–K), the DENV4 NS1 dimer is colored light and dark gray; the ZIKV NS1 dimer is colored wheat and orange. The designed binders D4NB4, D4NB11, and ZNB6 are colored green, blue, and violet, respectively.

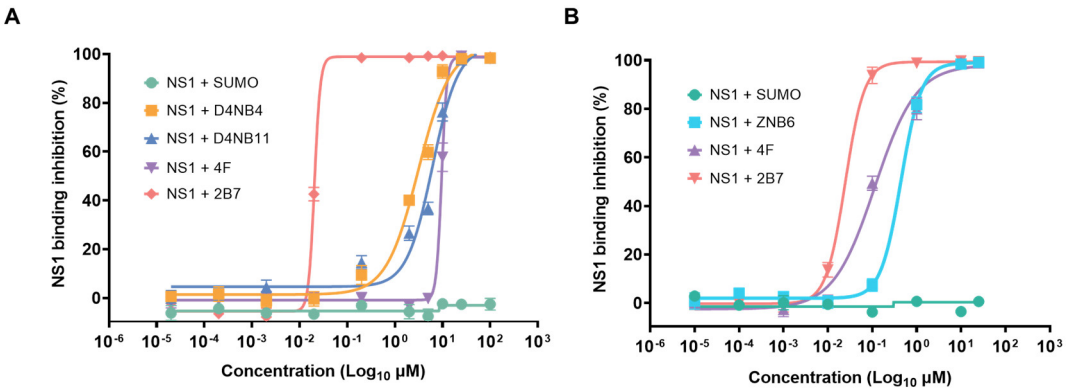

C

IC_{50} (μM)	DENV4 NS1	ZIKV NS1
D4NB4	3.09	-
D4NB11	6.16	-
ZNB6	-	0.45
4F	9.56	0.11
2B7	0.02	0.02

Figure 5. Inhibition of DENV4 and ZIKV NS1 binding to target cells by designed protein binders.

(A) Inhibition of DENV4 NS1 binding to HBMECs by protein binders D4NB4 and D4NB11.

(B) Inhibition of ZIKV NS1 binding to HUVECs by protein binder ZNB6.

(C) IC_{50} values of protein binders against DENV4 and ZIKV NS1 binding to target cells.

Table S1. *In silico* validation scores of selected designs.

Design	RMSD (Å)	pLDDT	pAE (Å)	ipTM	Length (aa)	Mr (Da)
D4NB1	0.508	92.265	6.580	0.85	116	13486.91
D4NB2	0.812	91.182	7.346	0.86	152	16384.00
D4NB3	0.596	92.340	6.337	0.83	73	8026.13
D4NB4	0.592	93.746	6.193	0.83	110	11904.86
D4NB5	0.988	88.822	7.955	0.86	109	12133.00
D4NB6	0.927	87.295	9.310	0.82	116	11729.60
D4NB7	0.778	90.303	7.053	0.87	139	16382.50
D4NB8	0.927	89.404	7.730	0.83	87	9754.31
D4NB9	0.678	92.069	6.466	0.83	110	12780.15
D4NB10	0.977	92.360	6.947	0.83	128	13933.35
D4NB11	0.462	91.424	7.268	0.84	71	8291.52
D4NB12	0.956	92.047	6.586	0.85	78	8515.94
ZNB1	0.460	93.607	6.893	0.85	110	12132.97
ZNB2	0.564	90.837	5.869	0.83	88	9321.54
ZNB3	0.471	90.963	7.394	0.83	119	12673.56
ZNB4	0.697	93.800	7.191	0.82	98	10071.47
ZNB5	0.514	93.224	5.847	0.84	157	17389.13
ZNB6	0.812	88.773	7.263	0.84	79	8971.50
ZNB7	0.824	84.152	7.824	0.84	78	8946.25

Table S2. Statics of data collection, data process, model refinement, and validation.

	DENV4_NS1-D4NB4 (EMDB: 67018) (PDB: 9XMA)	DENV4_NS1-D4NB11 (EMDB: 67019) (PDB: 9XMB)	ZIKV_NS1-ZNB6 (EMDB: 67020) (PDB: 9XMC)
Data and processing			
Magnification	105,000	105,000	105,000
Voltage (kV)	300	300	300
Electron exposure (e^-/ Å^2)	49.40	48.42	49.14
Defocus range (μm)	-1.2 ~ -1.8	-1.2 ~ -1.8	-1.2 ~ -1.8
Pixel size (Å)	0.85	0.85	0.85
Symmetry imposed	C1	C1	C1
Initial particle images (no.)	4,952,298	9,362,396	2,040,256
Final particle images (no.)	132,236	106,756	107,034
Map resolution (Å)	3.0	3.0	3.5
FSC threshold	0.143	0.143	0.143
Map resolution range	2.8 - 4.5	2.8 - 4.5	3.2 - 5.0
Refinement			
Initial model used (PDB code)	-	-	-
Map sharpening B factor (Å^2)	70.74	49.80	76.61
Model composition			
Non-hydrogen atoms	5965	5921	6057
Protein residues	760	749	758
Ligands	-	-	-
B factor (Å^2)			
Protein	81.17	72.24	32.90
Ligand	-	-	-
R.m.s. deviations			
Bond lengths (Å)	0.004	0.002	0.003
Bond angles (°)	0.525	0.435	0.575
Validation			
MolProbity score	1.58	1.45	2.01
Clash score	4.08	3.69	8.77
Rotamers outliers (%)	0.00	0.47	0.00
Ramachandra plot			
Favored	94.27	95.81	90.51
Allowed	5.73	4.19	9.49
Outliers	0.00	0.00	0.00

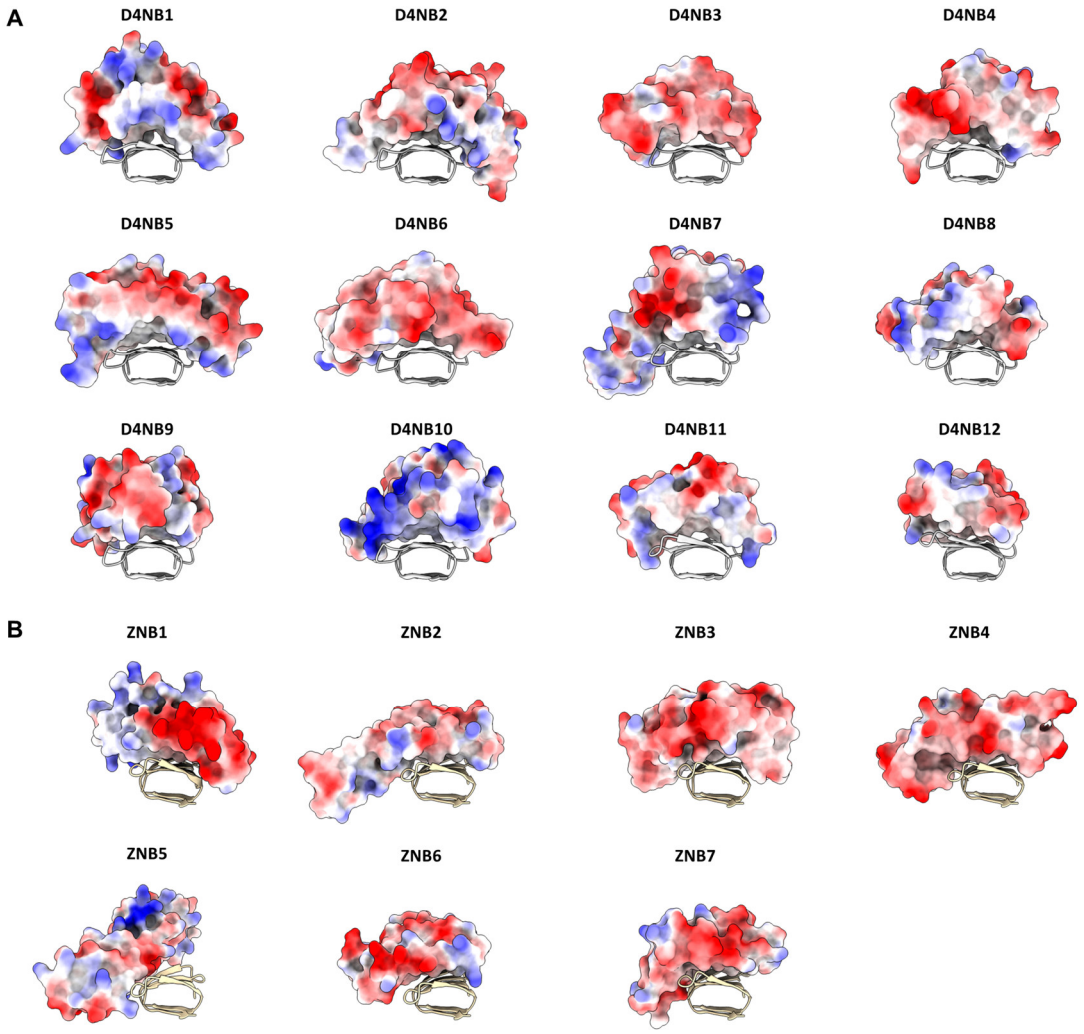

Figure S1. Shape complementarity between concave surfaces of designed protein binders and the convex β-roll domain of the NS1 dimer.

(A) Shape complementarity between the designed protein binders (surface, colored by electrostatic potential) and the β-roll domain of the DENV4 NS1 dimer (cartoon, colored light gray).

(B) Shape complementarity between the designed protein binders (surface, colored by electrostatic potential) and the β-roll domain of the ZIKV NS1 dimer (cartoon, colored wheat).

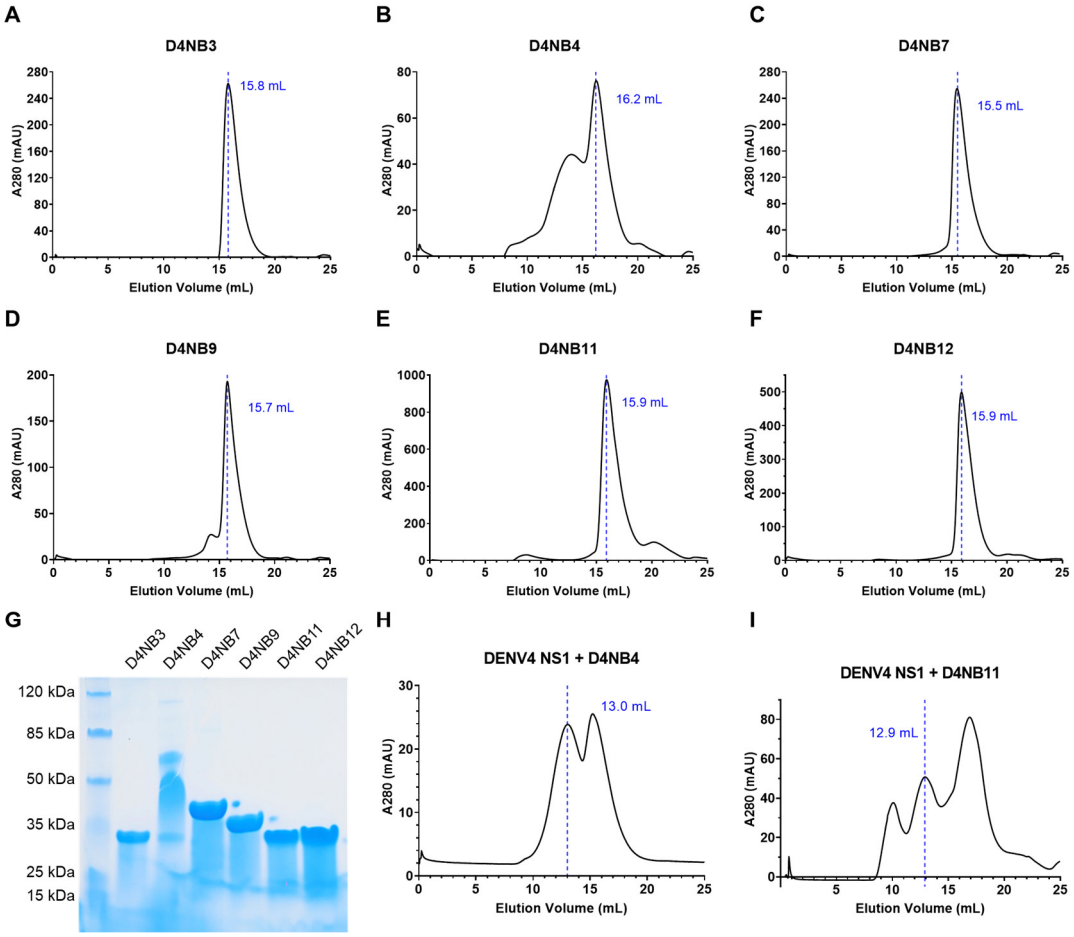

Figure S2. Purification of designed protein binders targeting the DENV4 NS1 dimer.

(A–F) Size-exclusion chromatography profiles of D4NB3, D4NB4, D4NB7, D4NB9, D4NB11, and D4NB12 on a Superdex 200 Increase column.

(G) SDS-PAGE analysis of purified protein binders D4NB3, D4NB4, D4NB7, D4NB9, D4NB11, and D4NB12.

(H, I) Size-exclusion chromatography profiles of DENV4 NS1 complexed with D4NB4 (H) and D4NB11 (I) on a Superdex 200 Increase column.

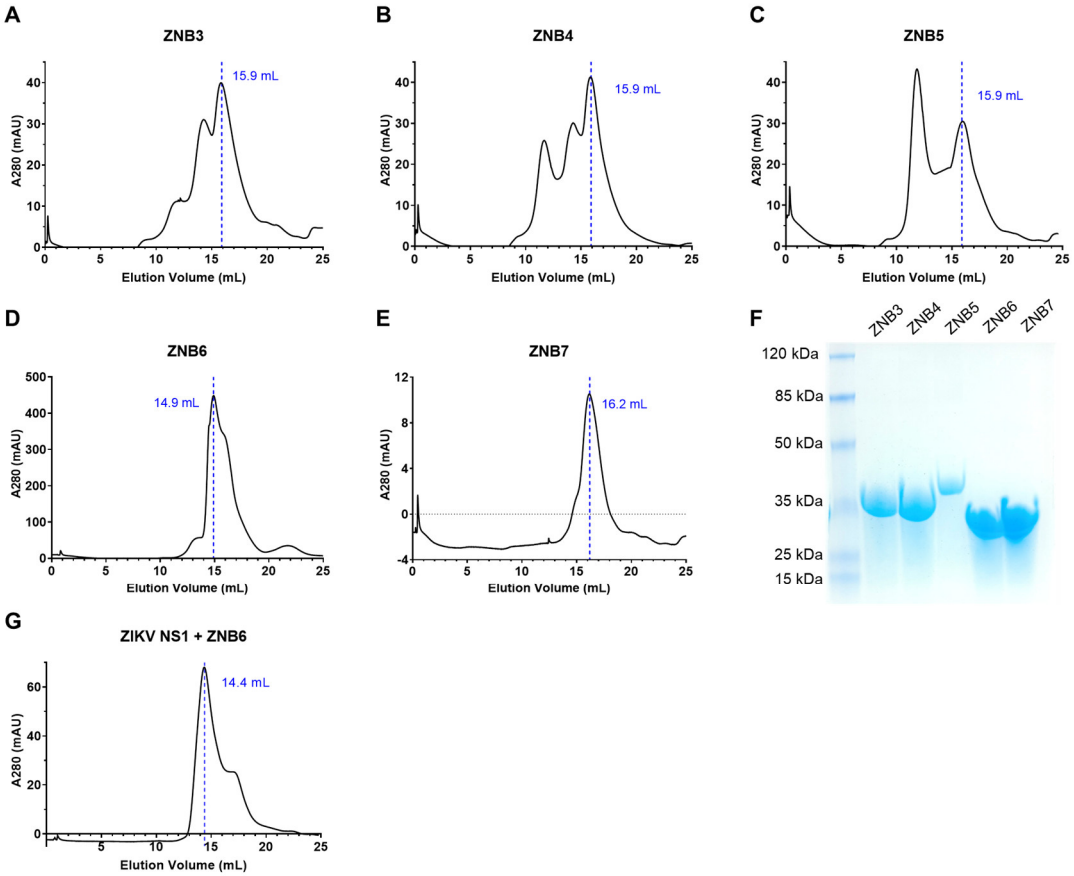

Figure S3. Purification of designed protein binders targeting the ZIKV NS1 dimer.

(A–E) Size-exclusion chromatography profiles of ZNB3, ZNB4, ZNB5, ZNB6, and ZNB7 on a Superdex 200 Increase column.

(F) SDS-PAGE analysis of purified protein binders ZNB3, ZNB4, ZNB5, ZNB6, and ZNB7.

(G) Size-exclusion chromatography profiles of ZIKV NS1 complexed with ZNB6 on a Superdex 200 Increase column.

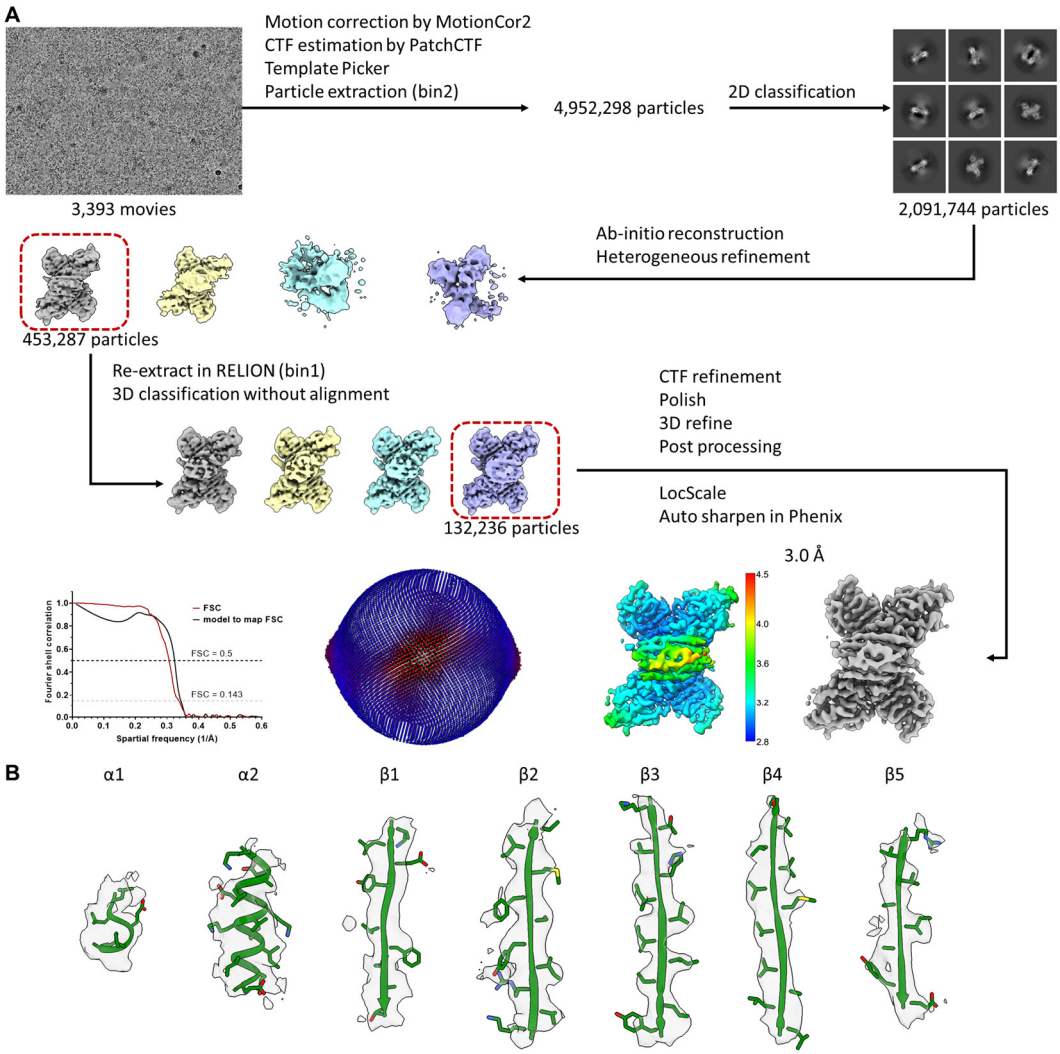

Figure S4. Cryo-EM data processing of the DENV4 NS1 dimer complexed with designed protein binder D4NB4.

(A) Cryo-EM data-processing pipeline for the DENV4_NS1–D4NB4 complex, including the angular distribution plot of refined particles and the gold-standard FSC curve.

(B) Electron densities for the secondary structure elements of D4NB4.

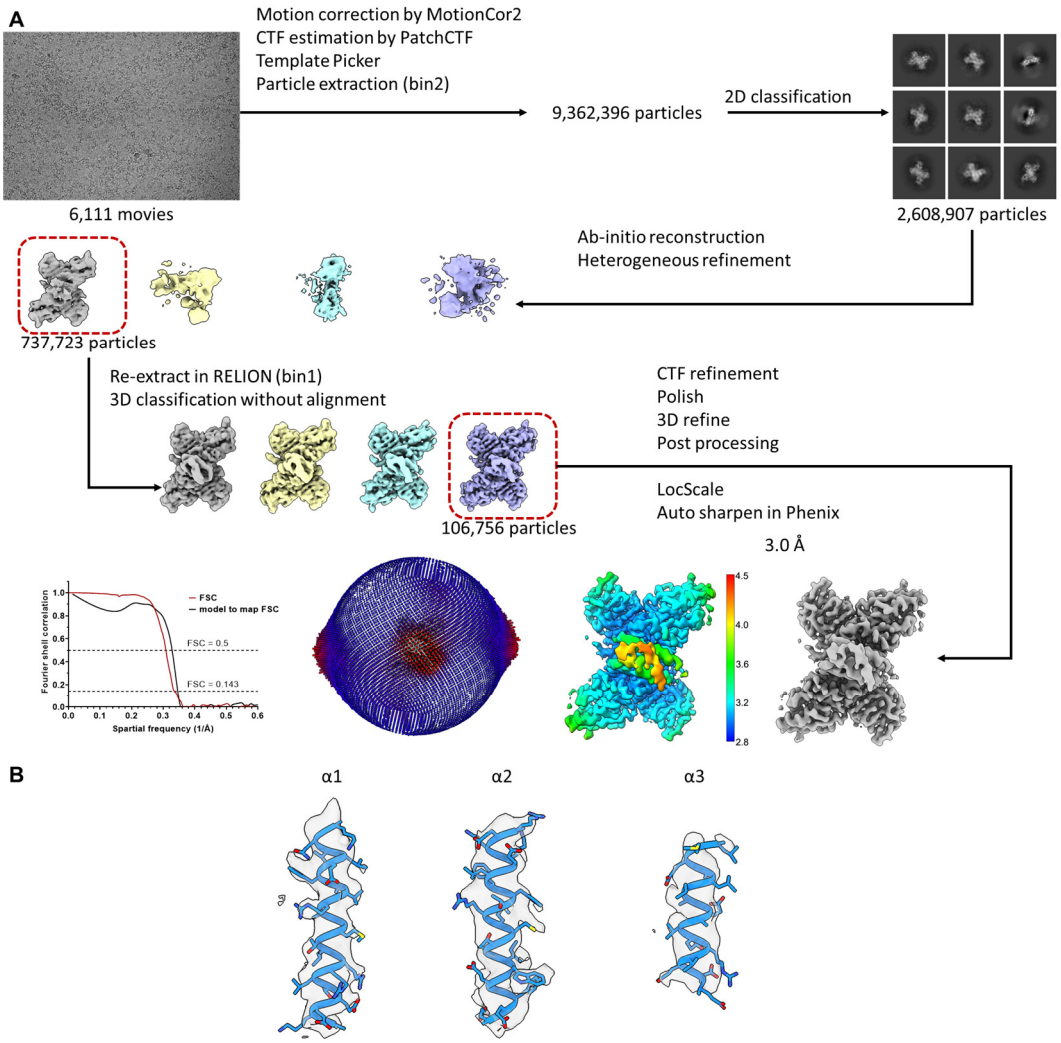

Figure S5. Cryo-EM data processing of the DENV4 NS1 dimer complexed with designed protein binder D4NB11.

(A) Cryo-EM data-processing pipeline for the DENV4_NS1–D4NB11 complex, including the angular distribution plot of refined particles and the gold-standard FSC curve.

(B) Electron densities for the secondary structure elements of D4NB11.

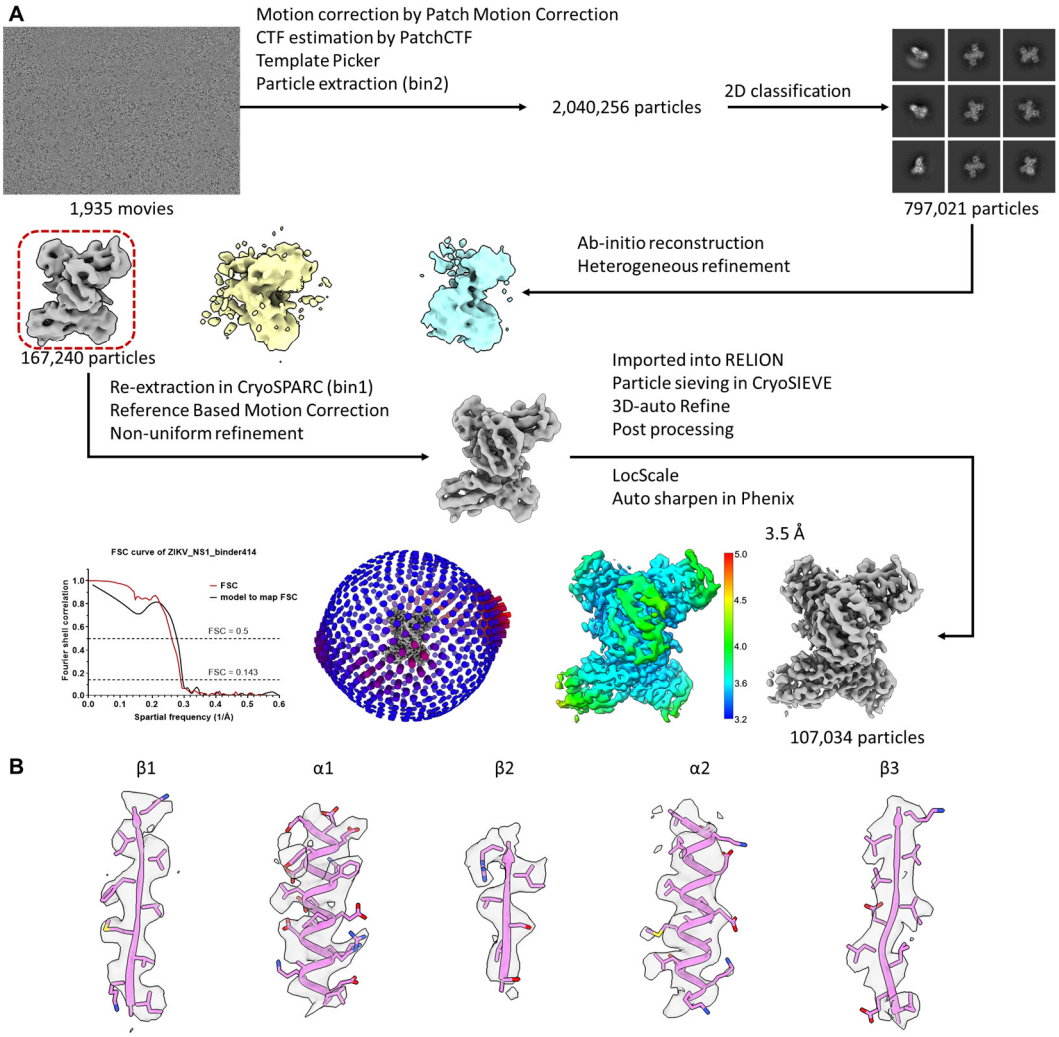

Figure S6. Cryo-EM data processing of the ZIKV NS1 dimer complexed with designed protein binder ZNB6.

(A) Cryo-EM data-processing pipeline for the ZIKV_NS1–ZNB6 complex, including the angular distribution plot of refined particles and the gold-standard FSC curve.

(B) Electron densities for the secondary structure elements of ZNB6.

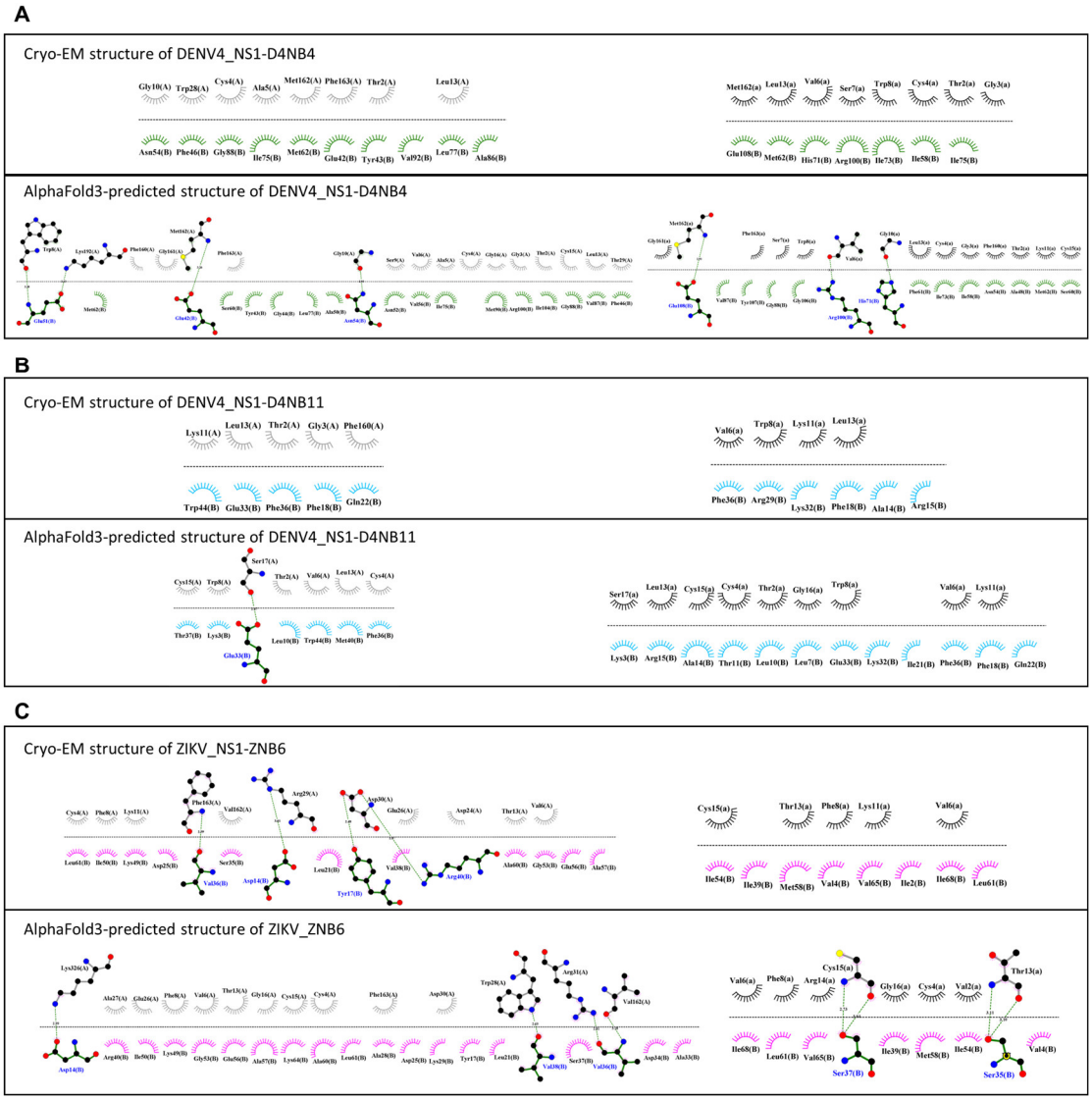

Figure S7. Interaction analysis between protein binders and the NS1 dimer using LigPlot^{+}.

(A) Interactions between D4NB4 (green bonds) and the DENV4 NS1 dimer (gray bonds) in the cryo-EM structure and the AlphaFold3 predicted model.

(B) Interactions between D4NB11 (blue bonds) and the DENV4 NS1 dimer (gray bonds) in the cryo-EM structure and the AlphaFold3 predicted model.

(C) Interactions between ZNB6 (violet bonds) and the ZIKV NS1 dimer (orange bonds) in the cryo-EM structure and the AlphaFold3-predicted model.

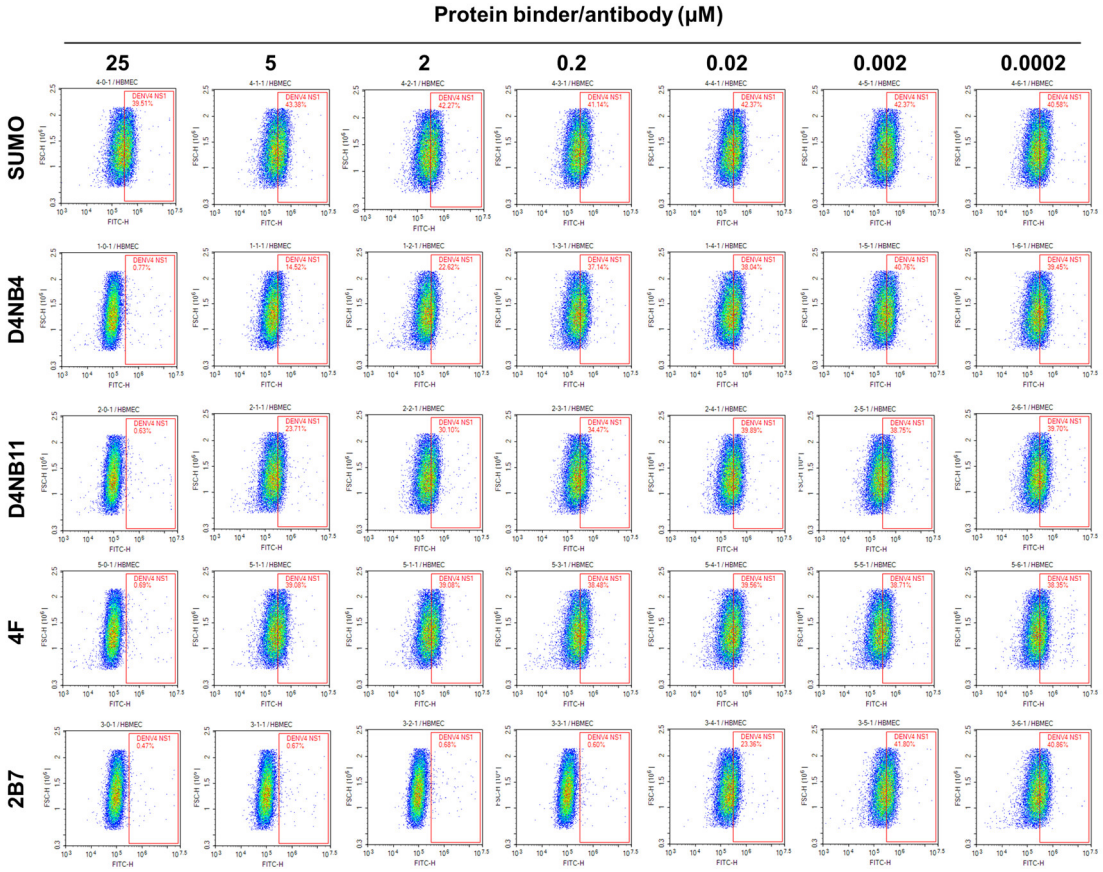

Figure S8. Flow cytometric analysis of DENV4 NS1 binding inhibition to HUVECs by protein binder D4NB4 and D4NB11 at varying concentrations.

.

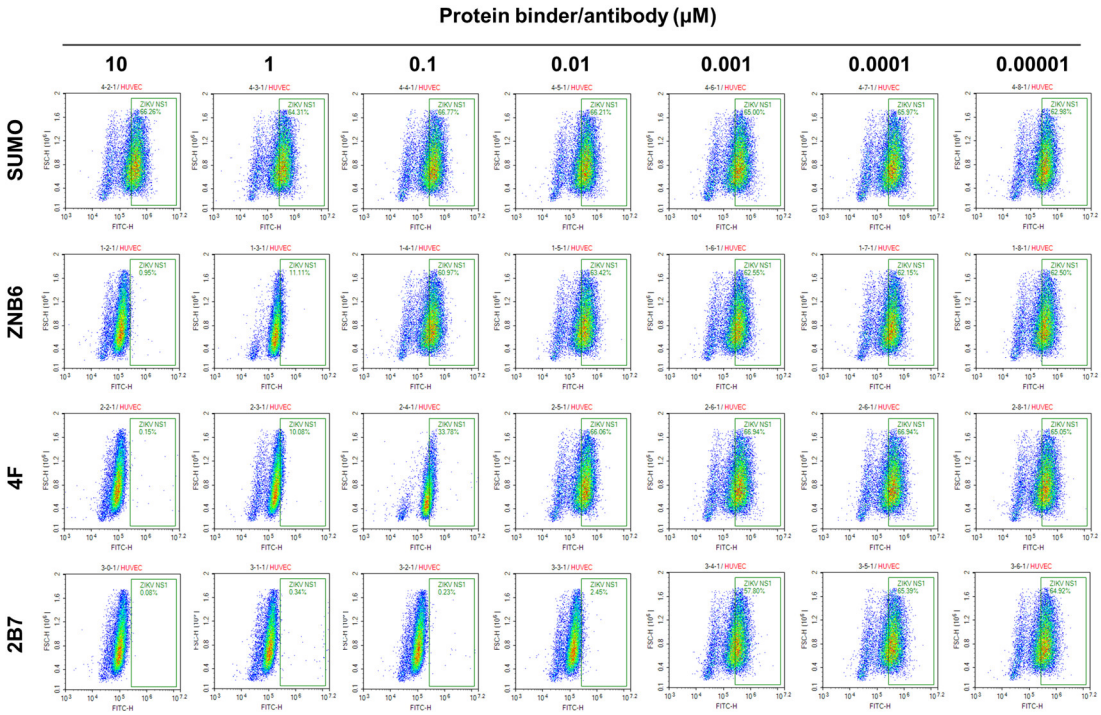

Figure S9. Flow cytometric analysis of ZIKV NS1 binding inhibition to HUVECs by protein binder ZNB6 at varying concentrations.